Supporting Information

An oxygen vacancy-modulated bifunctional S-$NiMoO_4$ electrocatalyst for efficient alkaline overall water splitting

Jiarong Mu[a], Ping Bai[a], Peng Wang[a], Zhinan Xie[a], Yihua Zhao[a], Jianfang Jing *[a], Yiguo Su *[a]

Materials and methods

Chemicals:

All chemicals used are analytically pure, no further purification is performed. Ethanol [(C_2H_5OH), ⩾99.7%] hydrochloric acid [(HCl), 37%] nickel nitrate hexahydrate [($Ni(NO_3)_2·6H_2O$), 98%] ammonium molybdate [($(NH_4)_6Mo_7O_{24}·4H_2O$), 98%] and urea [($C_2H_5NO_2$), 99%] were choosed from Tianjin Fengchuan Chemical Reagent Co. Ltd., China. Thioacetamide [(C_2H_5NS), 99%] ammonium fluoride [(NH_4F), 99%] Nickel foam (NF) were purchased from Beijing Innochem Technology Co., Ltd. Potassium hydroxide [(KOH), 99.99%] iridium oxide powder [(IrO_2), 99%], and platinum powder (Pt, 20wt%) were obtained from Alfa Aesar.

Pretreatment of NF:

In 3 mol L^{-1} HCl solution, the 3×4 cm NF was ultrasonic treatment 30 minutes to wipe out oxides, then apply sonication in acetone for 30 minutes for grease removal, and finally ultrasonically washed with C_2H_5OH and Deionized water (DI H_2O) for five times, and then dried at 50 °C for 3h that under vacuum.

Synthesis of $NiMoO_4$/NF precursor:

$Ni(NO_3)_2·6H_2O$ (0.5816 g), $(NH_4)_6Mo_7O_{24}·4H_2O$ (0.61793 g) and NF were dissolved ultrasonically in 50 mL of DI H_2O and reacted under hydrothermal conditions at 120 °C for 8 hours. Following cooling, the resultant product had washed 3 times with DI water and C_2H_5OH before being vacuum-dried at 50 °C for 3 hours to yield $NiMoO_4$/NF.

Synthesis of S-$NiMoO_4$/NF precursor:

Dissolve 150 mg of C_2H_5NS in a 50 mL Teflon autoclave containing 35 mL of C_2H_5OH and sonicate for 30 minutes, and put into a piece of $NiMoO_4$/NF precursor, which was reacted for 5 h at 120 °C. Following cooling, the resultant product had washed 3 times with DI H_2O and C_2H_5OH before being vacuum-dried at 50 °C for 3 hours to yield S-$NiMoO_4$/NF.

Synthesis of S-Ni/NF, S-Mo/NF, S/NF precursor:

$Ni(NO_3)_2 \cdot 6H_2O$ (0.5186 g), NH_4F (0.1481 g), $C_2H_5NO_2$ (0.6004 g) was ultrasonically decentralized in 30 mL of DI water, moreover, $(NH_4)_6Mo_7O_{24} \cdot 4H_2O$ (0.61793 g) was ultrasonically decentralized in 30 mL of DI water, and put into NF, reacted under hydrothermal conditions at 120 °C for 8 hours. Following cooling, the resultant product had washed 3 times with DI H_2O and C_2H_5OH before being vacuum-dried at 50 °C for 3 hours to yield NiOOH/NF and $Mo(OH)_3$/NF. Dissolve 150 mg C_2H_5NS in 35 mL C_2H_5OH and sonicate for 30 minutes, put a piece of NiOOH/NF, $Mo(OH)_3$/NF and a clean NF, respectively, and solvent heat reaction at 120 °C for 5 hours. Following cooling, the resulting product was washed 3 times with DI water and C_2H_5OH before being vacuum-dried at 50 °C for 3 hours to yield S-Ni/NF, S-Mo/NF, and S/NF.

All the above hydrothermal reactions were carried out in a 100 mL Teflon autoclave, and all of the solvent-thermal reactions were carried out in a 50 mL Teflon autoclave. Technical abbreviations are expanded upon when first used.

Synthesis of 20 wt% Pt/C/NF:

First, 5.0 mg of 20 wt% Pt/C catalyst was dispersed in 100 µL of ethanol and 10 µL of Nafion solution using magnetic stirring for 10 hours to create a uniform ink. Next, the ink was dripped slowly onto a clean NF surface and air-dried.

Synthesis of IrO_2/NF:

5.0 mg of IrO_2 catalyst was dispersed in 100 µL of ethanol and 10 µL of Nafion solution using magnetic stirring for 10 hours to create a uniform ink. Next, the ink was dripped slowly onto a clean NF surface and air-dried.

Materials characterization:

X-ray diffraction (XRD) was measured to analyze the crystal structure. Test conditions: scan range and scan rate: 5 ° - 80 ° and 4.5 ° min^{-1}, respectively, using Kα rays, λ=0.15406. Scanning Electron Microscope with Field Emission (Hitachi S-4800 type, Japan) characterization technique was used to morphology analysis and surface texture and dimensions of the synthesized catalysts. Scanning electron microscopy (SEM) is used to study the topographical features, size, and distribution of different samples. High-resolution transmission electron microscopy (TEM: FEI Tecnai G2 F20 S-TWIN, 200 kV) was used to research the lattice structure, morphology, and particle size of the synthesized catalysts. Qualitative and quantitative analyses of the synthesized catalysts were performed by X-ray photoelectron spectroscopy characterization (XPS) for valence, defects, elemental content, etc. It was also calibrated with C 1s line at 284.6 eV. ICP-MS measured element contents on an Agilent 7700. Oxygen vacancy content of different catalysts tested by electron paramagnetic resonance (EPR).

Electrochemical measurement:

The electrochemical properties of all catalysts were tested using CHI760E electrochemical workstation. In the standard three-electrode system, the working electrode was a nickel foam (NF) containing the catalyst, the reference electrode used in the experiment was Ag/AgCl, while a platinum mesh electrode was the counter electrode. All of the potentials were subjected to 90% iR correction. They were then converted into a reversible hydrogen electrode (RHE) using method $E_{RHE} = 0.1976 + 0.059 \times pH + E_{Ag/Agcl}$.

Electrochemical impedance spectroscopy (EIS) was performed at 5 mV^{-1} amplitude, 0.01 Hz to 100 kHz frequency, and 0.35 V potential relative to RHE. All technical abbreviations were clarified upon their initial use. To determine the effective electrochemically active surface area (ECSA), the double-layer capacitance (C_{dl}) curves were tested at multiple scanning speeds within the non-Faraday current districts, with HER potentials scoping from -0.8 to -0.85 V (vs. RHE) and OER potentials ranging from 0.05 V to 0.1 V (vs. RHE). Catalyst stability was assessed using the chronopotential (CP) method.

Overall water splitting tests:

The LSV curves of overall water splitting (OWS) test were conducted on CHI760E electrochemical workstation. A 1 M KOH electrolyte solution was used to fully simulate the overall water splitting system. The electrolytic cell consisted of two identical pieces of S-$NiMoO_4$/NF functioning as the cathode and anode.

It can be seen intuitively that the nickel foam experienced color changes from silver, yellow, to black during the two-step hydrothermal process (**Fig. S1**), indicating the successful formation of S-$NiMoO_4$/NF catalyst.

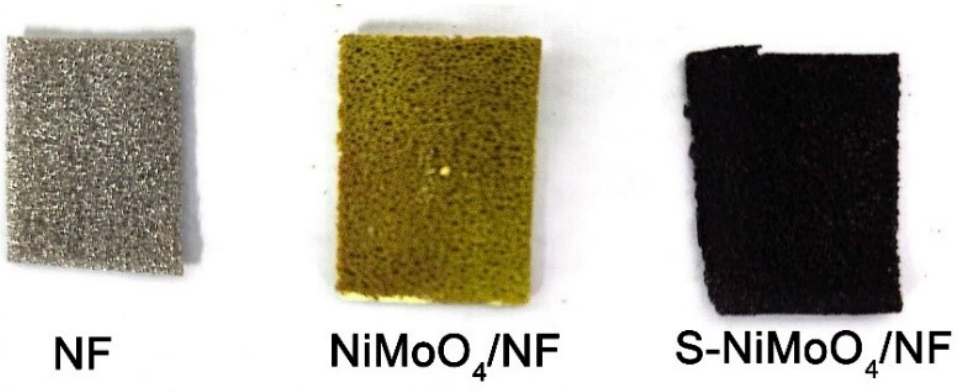

Fig. S1. Photographs of NF, $NiMoO_4$/NF and S-$NiMoO_4$/NF

Catalyst morphology analysis:

The SEM images of the two samples, precursor $NiMoO_4$/NF and S-$NiMoO_4$/NF, at different magnifications were shown in **Fig. S2**. It could be analyzed that before sulfidation, the samples were mainly $NiMoO_4$ nanorods single crystals grown on nickel foam, as shown in **Fig. S2a, b and c**, the SEM images showed that $NiMoO_4$ growed

on top of the nickel foam regularly and uniformly, with a neat and regular rod structure and a large size, and with the introduction of S-atoms, the basic morphology did not change, and the crosslinked nanorods were retained intact, and the crosslinked nanorods were retained completely. As shown in **Fig. S2d, e and f**, the spherical particles appeared uniformly on the nanorods, and the SEM images with different magnifications clearly showed that the introduction of S atoms changed the specific surface area of the precursor, because of more active sites could be exposed, which were favorable for the transfer of protons and electrons.

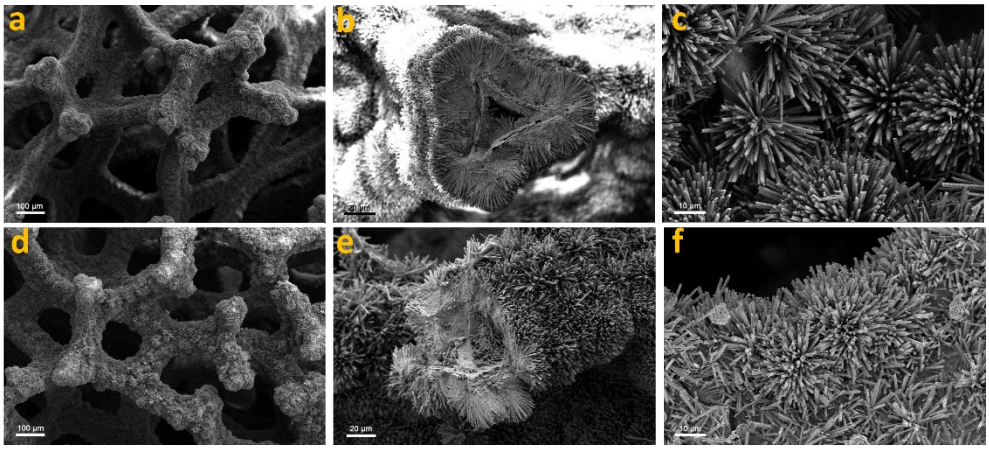

Fig. S2. SEM images (**a-c**) of $NiMoO_4$/NF precursor, SEM images (**d-f**) of S-$NiMoO_4$/NF precursor.

Results and discussion

Catalyst synthesis and characterization

The ICP (**Fig. S3**) test was like the EDS and after analysis, the mass fraction of elemental Mo was 27.7357%, elemental Ni is 38.01% and elemental S was 3.8675%.

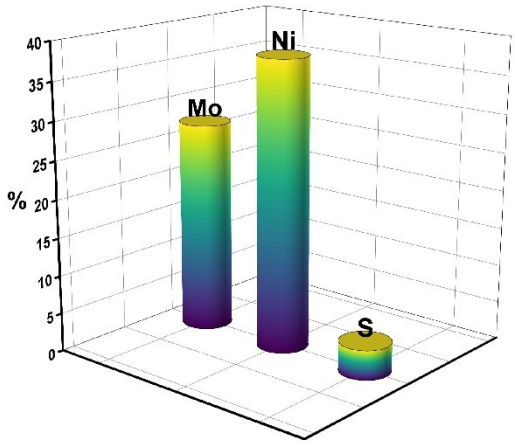

Fig. S3. ICP image of S-$NiMoO_4$/NF precursor.

Fig. S4a confirmed the coexistence of Ni, Mo, S and O in the S-$NiMoO_4$/NF catalyst. **Fig. S4b** showed the 2p orbital spectra of S. After vulcanization, the XPS showed three characteristic peaks at 161.41 eV (Ni-S bond), 162.66

eV (Mo-S bond), and 167.18 eV (S-O bond), and the first two characteristic peaks were the $2p_{3/2}$ S orbitals, and the last one was the characteristic peak of the S-O bond, and the XPS of S fully indicated the successful doped of the S element.

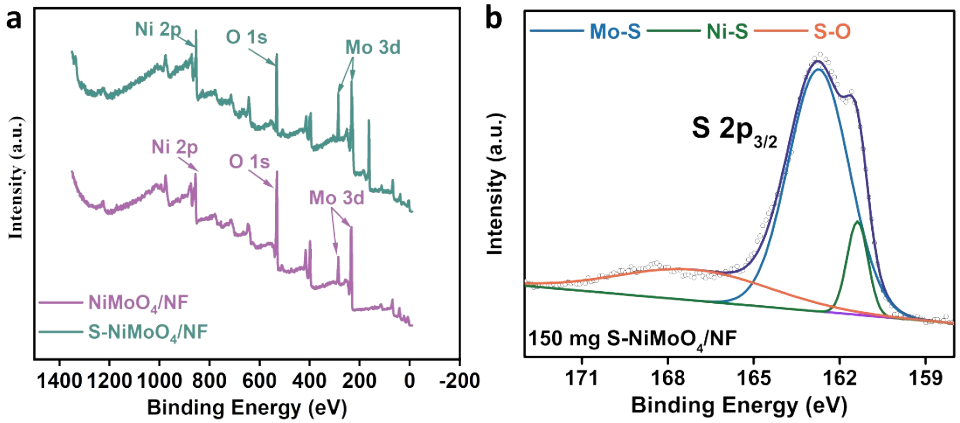

Fig. S4. (**a**) XPS survey of $NiMoO_4$/NF and S-$NiMoO_4$/NF catalysts, (**b**) High-resolution XPS spectra of S 2p.

In addition, we compared the effect of different S-doping amounts on S-$NiMoO_4$/NF in **Fig. S5**, where 150 mg of S-doping forms the optimal ratio of Ni and Mo valence states, as well as the formation of the most oxygen vacancies. These results indicated that a moderate amount of S-doping could well control the content of oxygen vacancies and thus enhanced the electrochemical performance. As one of the intrinsic defects of metal oxides, the concentration of oxygen vacancies and their distribution had their important effects on the bulk phase (e.g., electrical conductivity, material energy band structure, etc.) and surface (e.g., surface composition, molecular adsorption, etc.) of metal oxides, which could promote electron migration and enhanced the electrical conductivity. The **Fig. S5** had been increasing with the increase of S-doping, and 150 mg S-doping possessed an optimal oxygen vacancies content and an electrocatalytic performance. But when doped with 200 mg, the new structure generated (**Fig. S5d**), which may be unfavorable to performance.

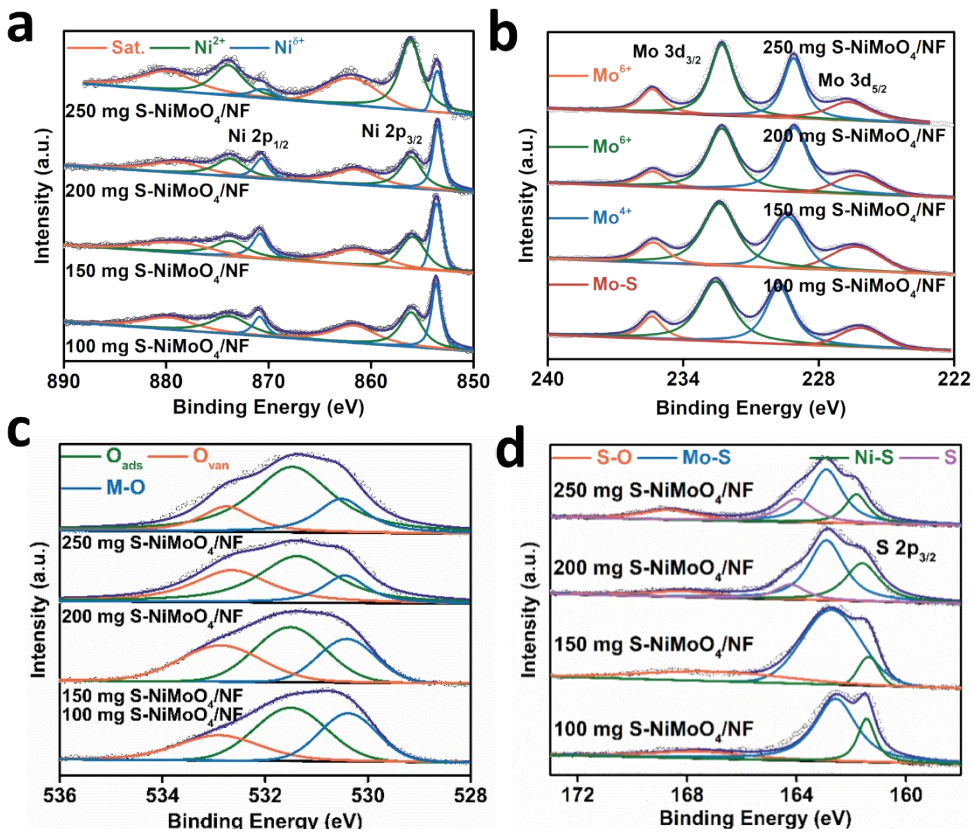

Fig. S5. XPS spectra of (**a**) Ni 2p, (**b**) Mo 3d, (**c**) O 1s, (**d**) S 2p of different sulfur doping levels S-$NiMoO_4$/NF catalysts.

The vacancy/lattice oxygen ratio **(Fig. S6)** increased with increasing S-doping, but according to the XPS spectroscopy results, when S-doping reached 200 mg, a new structure is created, which had some effect on the performance, so 150 mg S-doping produced the best oxygen vacancy ratio.

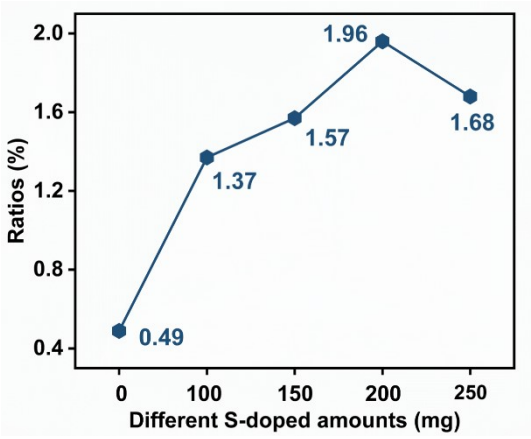

Fig. S6. The ratio of oxygen vacancies/lattice oxygen.

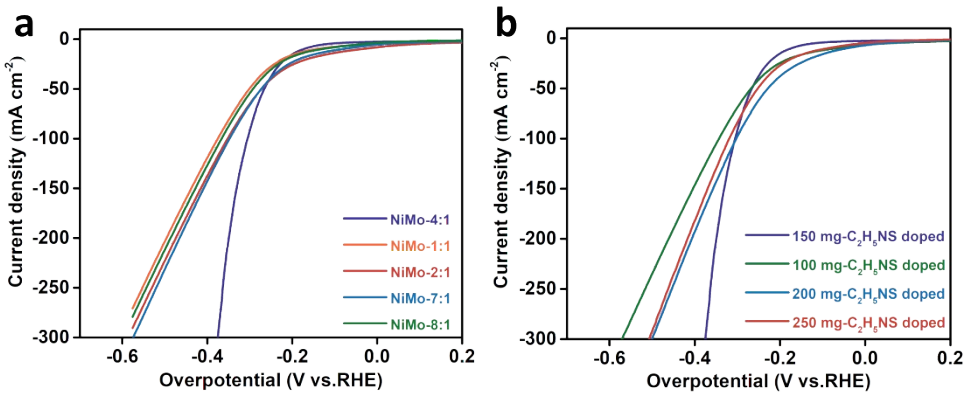

Fig. S7. LSV curves for HER of S-$NiMoO_4$/NF catalysts (**a**) with different Ni-Mo ratios and (**b**) with different sulfur doping

In addition, **Fig. S7a** showed the HER activity of S-$NiMoO_4$/NF catalysts synthesized with different ratios of nickel nitrate and ammonium molybdate, where S-$NiMoO_4$/NF with a nickel to molybdenum ratio of 4:1 found the optimum ratio in the reactants, and **Fig. S7b** showed that the introduction of 150 mg of C_2H_5NS maximized the HER performance.

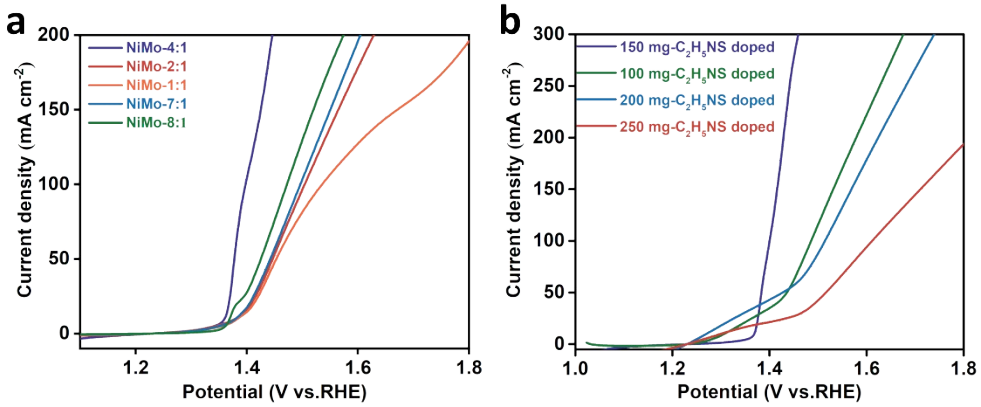

Fig. S8. LSV curves for OER of S-$NiMoO_4$/NF catalysts (**a**) with different Ni-Mo ratios and (**b**) with different sulfur doping

In addition, **Fig. S8a** showed the OER activity of S-$NiMoO_4$/NF catalysts synthesized with different ratios of nickel nitrate and ammonium molybdate, where S-$NiMoO_4$/NF with a nickel to molybdenum ratio of 4:1 found the optimum ratio in the reactants, and **Fig. S8b** showed that the introduction of 150 mg of C_2H_5NS maximized the OER performance.

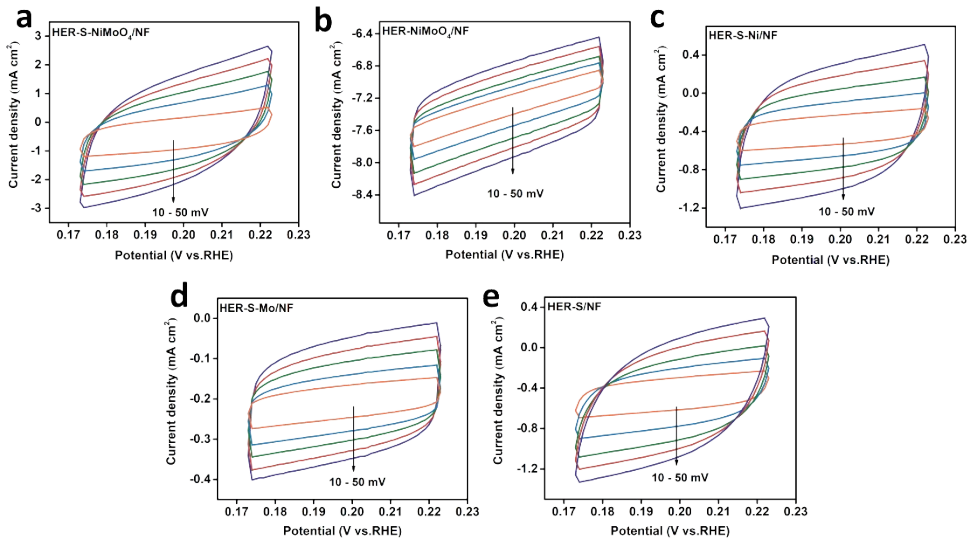

Fig. S9. CV curves of (**a**) S-$NiMoO_4$/NF, (**b**) $NiMoO_4$/NF, (**c**) S-Ni/NF, (**d**) S-Mo/NF and (**e**) S/NF in the non-faradaic capacitance current range.

Based on CV curves, the non-faradaic capacitance (C_{dl}) is the key index for detecting the ECSA. **Fig. S9** showed the CV curves of S-$NiMoO_4$/NF, $NiMoO_4$/NF, S-Ni/NF, S-Mo/NF, and S/NF catalysts under different scan rates from 10 to 50 $mV \cdot s^{-1}$ in the region of -0.80 to -0.85 V (vs. RHE).

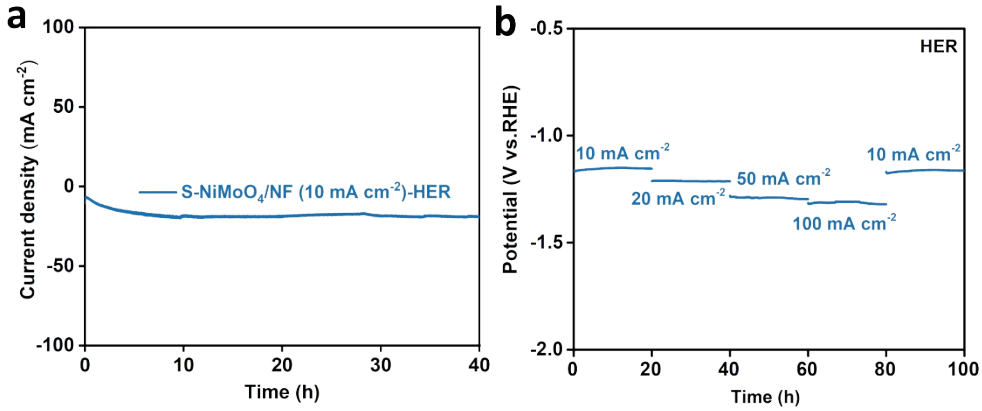

Fig. S10. (**a**) Chronoamperometry test of S-$NiMoO_4$/NF for HER, (**b**) Chronopotentiometry responses of S-$NiMoO_4$/NF at various current densities for HER.

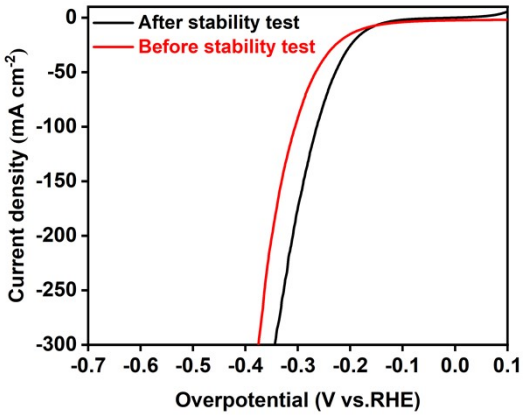

Fig. S11. LSV before and after HER cycling test.

LSV comparisons of catalysts before and after HER stabilization were performed, after the cycling test, the LSV exhibited a slight shift **(Fig. S11)**.

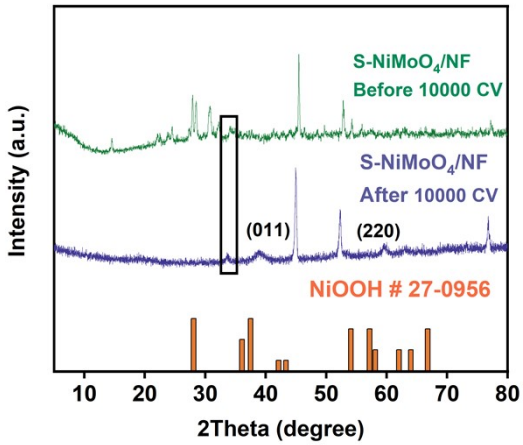

Fig. S12. XRD before and after HER cycling test.

XRD (**Fig. S12**) showed a decrease in the crystallinity of the catalyst. The appearance of new characteristic peaks corresponded to the (011) and (220) crystal planes of NiOOH in standard card (JCPDS, No. 27-0956).

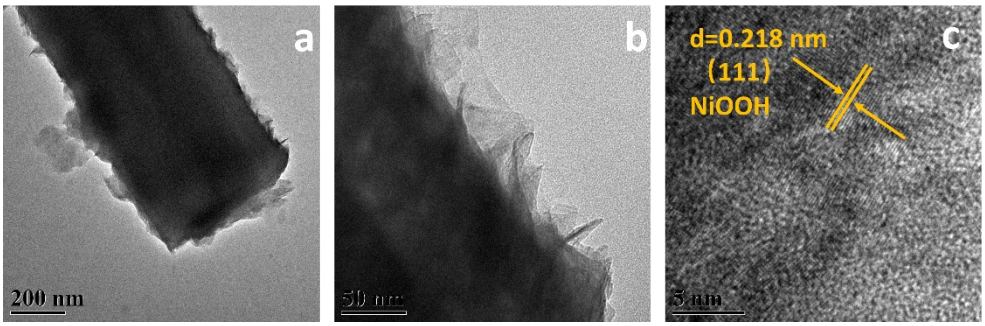

Fig. S13. TEM images of S-$NiMoO_4$/NF catalysts after HER stability test.

TEM (**Fig. S13**) showed that the reconfiguration process preserved the morphology of the nanorods, with lamellar NiOOH appearing at the edges. The lattice fringe of 0.218 nm, was corresponded to the (111) plane of NiOOH.

XPS results confirmed the leaching of Mo and S (**Fig. S14**). In the XPS of Ni 2p, new characteristic peaks attributed to Ni^{3+} at 876.84 eV and 858.77 eV were observed, [1] which confirmed the catalyst reconstruction to Ni-based hydroxide. The observed Mo^{6+} proved Mo element was only partially leached. The disappearance of XPS signal of S 2p showed that S was completely leached.

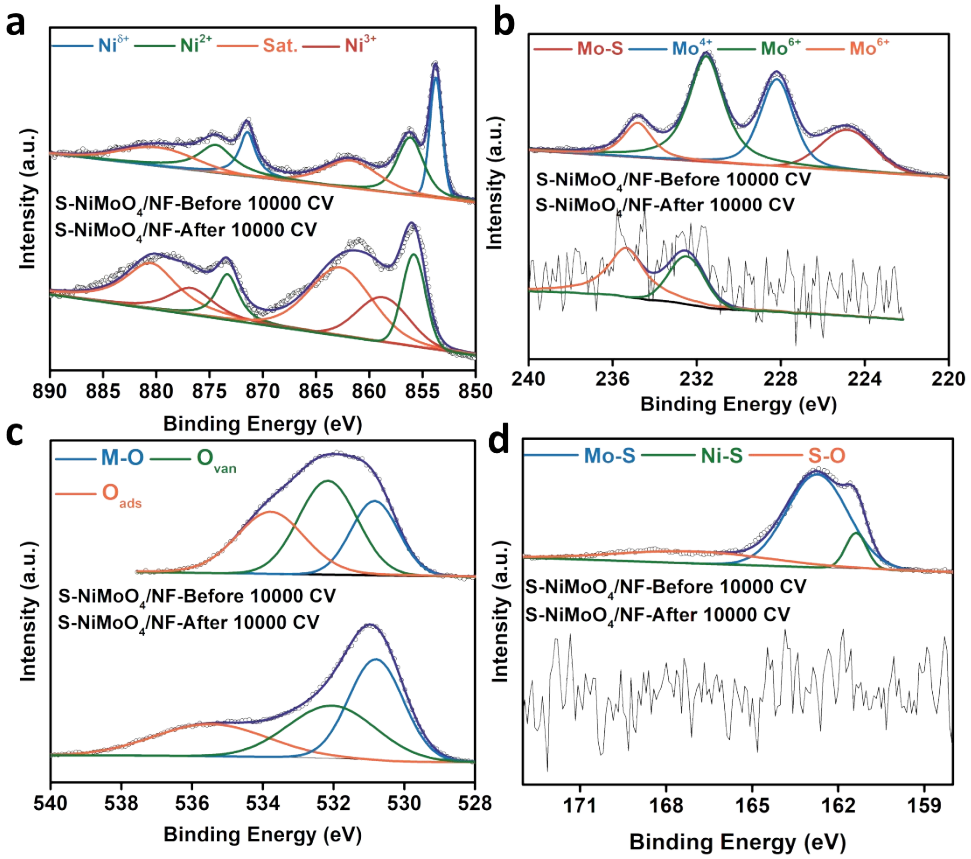

Fig. S14. Structural characterizations. High-resolution XPS spectra of (**a**) Ni 2p, (**b**) Mo 3d, (**c**) O 1s, (**d**) S 2p of S-$NiMoO_4$/NF catalysts before and after HER stability test.

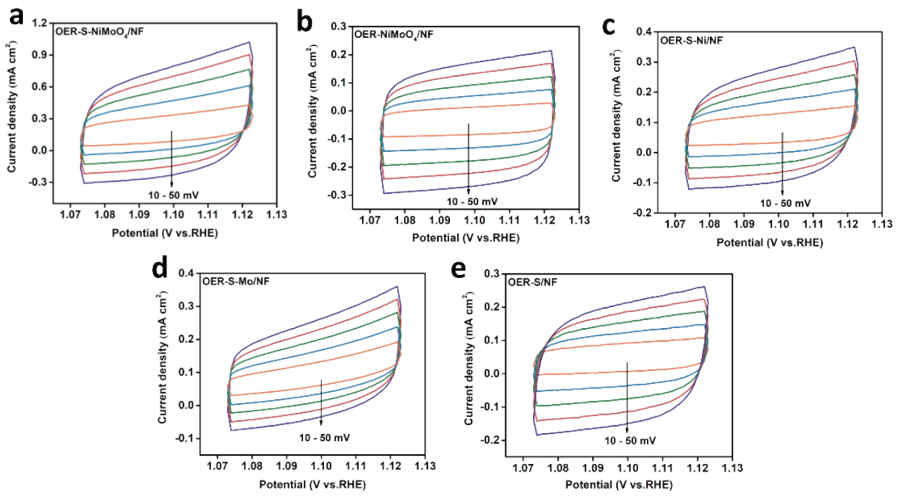

Fig. S15. CV curves of (**a**) S-$NiMoO_4$/NF, (**b**) $NiMoO_4$/NF, (**c**) S-Ni/NF, (**d**) S-Mo/NF and (**e**) S/NF in the non-faradaic capacitance current range.

Based on CV curves, the non-faradaic capacitance (C_{dl}) is the key index for detecting the ECSA. **Fig. S15** showed the CV curves of S-$NiMoO_4$/NF, $NiMoO_4$/NF, S-Ni/NF, S-Mo/NF, and S/NF catalysts under different scan rates from 10 to 50 $mV \cdot s^{-1}$ in the region of 0.05 to 0.10 V (vs. RHE).

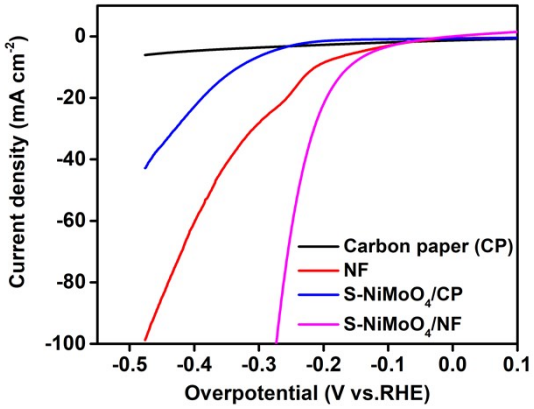

Fig. S16. HER LSV curves for CP, NF, S-$NiMoO_4$/CP and S-$NiMoO_4$/NF.

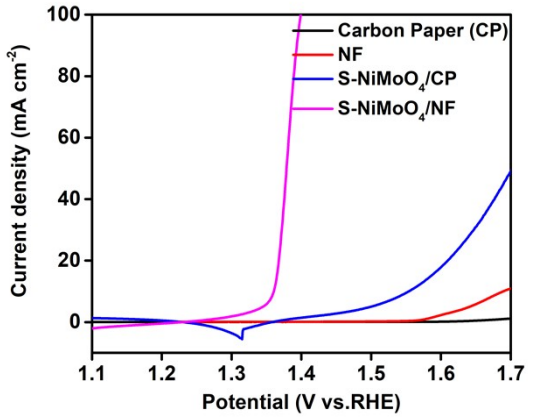

Fig. S17. OER LSV curves for CP, NF, S-$NiMoO_4$/CP and S-$NiMoO_4$/NF.

To demonstrate whether nickel foam contributes to the enhancement of OER and HER activities, we ultrasonically separated the S-$NiMoO_4$ on the S-$NiMoO_4$/NF catalysts and then weighed a 5 mg powder sample, which was homogeneously dispersed in a mixture of 100 μl of ethanol and 10 μl of Nafion. LSV curves were tested for pure carbon paper (CP), pure nickel foam (NF), and prepared catalysts coated on carbon paper (S-$NiMoO_4$/CP). The pure carbon paper showed no electrocatalytic activity, while loaded with S-$NiMoO_4$ on carbon paper (S-$NiMoO_4$/CP), the electrocatalytic activity improved. Further, when the S-$NiMoO_4$ grown on nickel foam (S-$NiMoO_4$/NF), the overpotentials of HER and OER were significantly lowered than that of pure nickel foam and S-$NiMoO_4$/CP (**Fig. S16, S17**), indicating that the nickel foam contributes to the improvement of electrocatalytic activity.

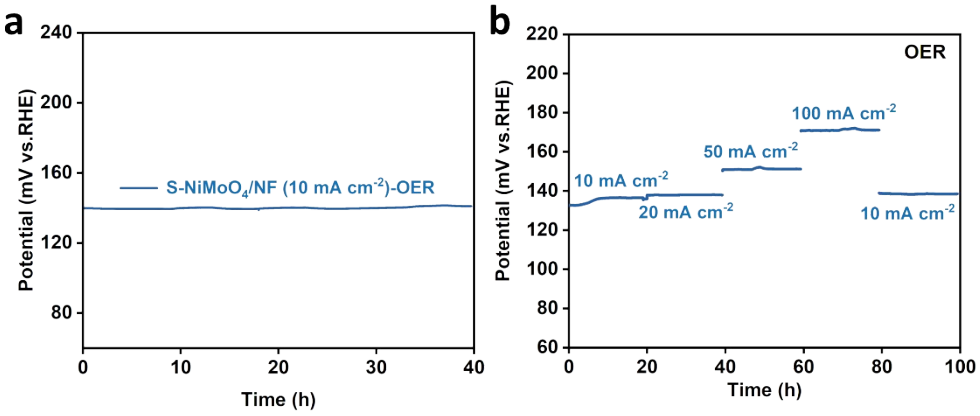

Fig. S18. Chronopotentiometry responses of S-$NiMoO_4$/NF at (**a**) 10 mA cm^{-2} and (**b**) various current densities for OER.

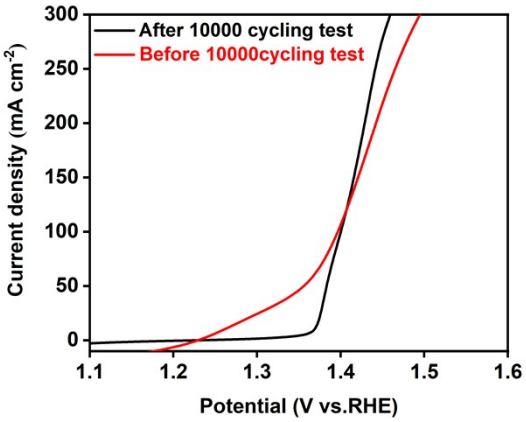

Fig. S19. LSV before and after OER cycling test.

Tested the LSV of S-$NiMoO_4$ after 10,000 CV cycles reveals that there was a slight enhancement in the performance of the catalyst at small current densities. This enhancement was negligible with the enhancement of current density. The OER performance decreased when the current density was greater than 150 mA cm^{-2}. **(Fig. S19)**

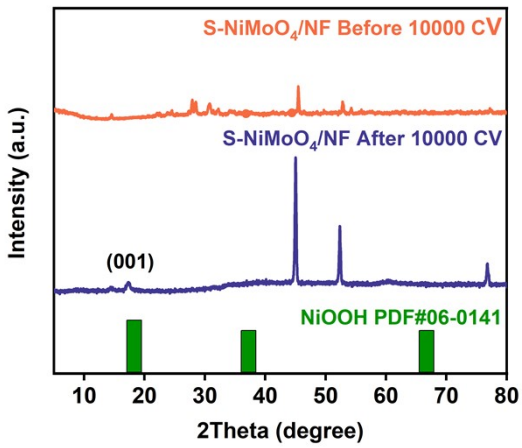

Fig. S20. XRD before and after OER cycling test.

XRD (**Fig. S20**) showed a decrease in the crystallinity of the catalyst, and new characteristic peaks appeared, corresponding to the (001) plane of NiOOH in standard card (JCPDS, No. 06-0141).

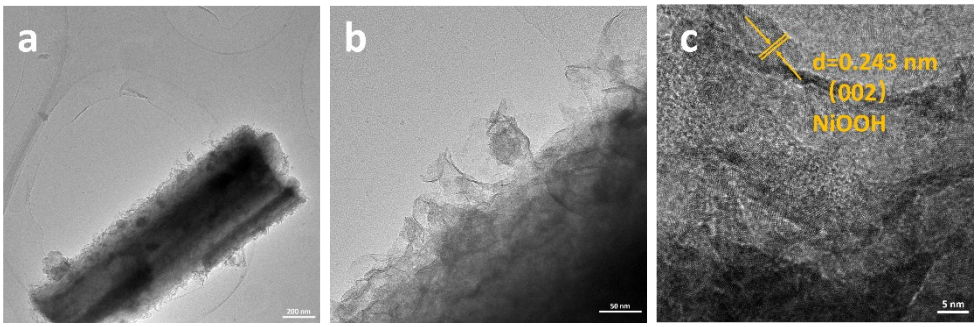

Fig. S21. TEM images of S-$NiMoO_4$/NF catalysts after OER cycling test.

TEM (**Fig. S21**) demonstrated that the reconfiguration process retained the nanorods morphology, with lamellar NiOOH appearing at the edges. The lattice spacing of 0.243 nm was assigned to the (002) crystallographic plane of NiOOH.

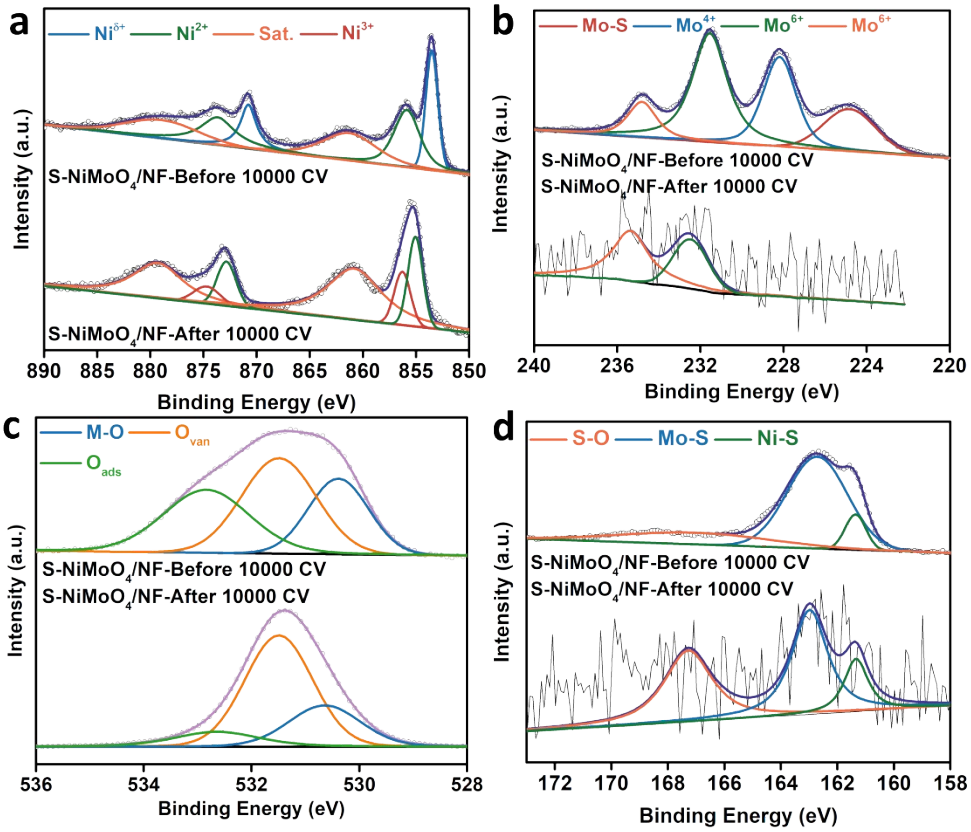

Fig. S22. Structural characterizations. High-resolution XPS spectra of (**a**) Ni 2p, (**b**) Mo 3d, (**c**) O 1s, (**d**) S 2p of S-$NiMoO_4$/NF catalysts before and after OER cycling test.

In the XPS of Ni 2p, new characteristic peaks at 874.69 eV and 856.28 eV belonged to Ni^{3+}, [2] which confirmed the catalyst reconfigured to Ni-based hydroxide (**Fig. S22a**). XPS of Mo 3d and S 2p results indicated the partial

leaching of Mo and S (**Fig. S22b, S22d**). Partial leaching of Mo and S elements resulted in a reduction of Mo-S bond. In addition, the reduction of Mo elements led to a decrease in lattice oxygen (**Fig. S22c**).

As well known, the leaching and reconfiguration of Mo-based catalysts is unavoidable. [3] Despite the occurrence of leaching led to reconfiguration in the S-$NiMoO_4$ catalyst, this reconfigured NiOOH can still serve as active sites for electrocatalytic water splitting. [4] As a result, the OER activity of S-$NiMoO_4$ catalyst can be maintained.

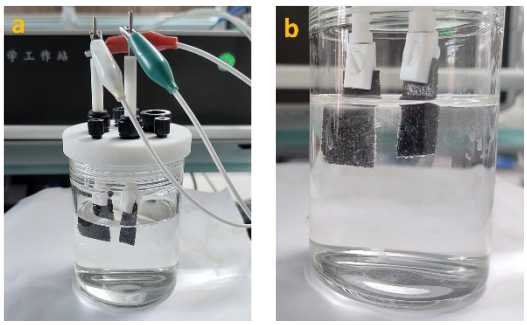

Fig. S23. Photographs during the overall water splitting.

In Fig. S23 and Movie. S1, the simulated total dewatering system experiment was shown, and the pictures as well as the video illustrate that the two-electrode system could perform both hydrogen and oxygen production, proving the real effectiveness of the total dewatering catalyst.

Table. S1. Peak area tables of oxygen vacancies and lattice oxygen.

Sample	O_{van}	M-O
S-$NiMoO_4$/NF	27196.96	17470.76
$NiMoO_4$/NF	23152.70	47350

S-doping into $NiMoO_4$ replaced some of the oxygen atoms and increased the oxygen vacancies, thus the O_{van} peak area increased. The decreased in lattice oxygen peak area was due to the removal of oxygen atoms from the lattice oxygen, which also proved the increase in oxygen vacancies. **(Table. S1)**

Table. S2. Comparison table of catalysts performance

Catalysts	Reaction /j	Overpotential(mV)	OWS/j (V)	Reference
S-$NiMoO_4$/NF	HER/50	235	1.55/50	This work
	OER/50	150		
Mo-NiCoP [5]	HER/10	76	1.61/10	Nano-Micro Lett. (2019) 11:15
	OER/10	269		

$Ni_{cluster}$-Ru NWs [6]	HER/10	17	1.454/10	Energy. Environ. Sci.
	OER/10	194		2021, 14, 3194-3202
$(Ru-Co)O_x$ [7]	HER/10	40	1.488/10	Angew. Chem. Int. Ed.
	OER/10	171		2020, 59, 17219-17224
CoFeZr oxides/NF [8]	HER/10	104	1.63/10	Adv. Mater.
	OER/10	264		2019, 31, 1901439
O-CoP [9]	HER/10	98	1.6/10	Adv. Funct. Mater.
	OER/10	310		2020, 30, 1905252
Ni_3N@2M-MoS_2 [10]	HER/50	97	1.64/50	Adv. Mater.
	OER/50	170		2022, 34, 2108505
NM-$MnCo_2O_4$/GDY [11]	HER/10	-	1.47/10	Adv. Funct. Mater.
	OER/10	338		2021, 32, 2107179
POM@ZnCoS/NF [12]	HER/10	170	1.56/10	Adv. Funct. Mater.
	OER/10	200		2021, 31, 2106147
Ni_3N-VN/NF [13]	HER/50	218	1.51/10	Adv. Mater.
Ni_2P-VP_2/NF [13]	OER/50	306		2019, 31, 1901174
Cr-doped-FeNi-P/NCN [14]	HER/10	190	1.50/10	Adv. Mater.
	OER/10	240		2019, 31, 1900178
MoS_2-AB/NF [15]	HER/10	77	1.51/10	Nano Energy
	OER/10	248		92(2022), 106707
$CoMoS_x$/NF [16]	HER/100	269	1.89/100	Angew. Chem. Int. Ed.
	OER/100	345		2020, 59, 1659-1665
Ni_5Co_3Mo-OH [17]	HER/10	52	1.43/10	ACS Energy Lett.
	OER/50	280		2019, 4, 952-959
Mo-NiP_xNiS_y [18]	HER/10	85	1.42/10	Adv. Funct. Mater.
	OER/10	1z37		2021, 31, 2101532
Ni-P-B/NF [19]	HER/50	76	1.661/50	Energy. Environ. Sci.
	OER/50	263		2020, 13, 102-110
$NiCo_2S_4$ [20]	HER/10	80	1.58/10	Adv. Funct. Mater.
	OER/10	243		2019, 29, 1807031

Author Contributions

Jiarong Mu: Conceptualization and designed the experiments, wrote the original draft, gave some suggestions, and

made deep discussion. **Ping Bai, Peng Wang, Zhinan Xie, Yihua Zhao:** Gave some suggestions and validation. **Jianfang Jing:** made deep discussion and revised the manuscript. **Yiguo Su:** Conceptualization, supervision, review, editing, made deep discussion and revised the manuscript. All authors discussed the results and commented on the manuscript.

References

1 H. Wang, L. Chen, L. Tan, X. Liu, Y. Wen, W. Hou and T. Zhan, *J. Colloid Interface Sci.*, 2022, **613**, 349-358.
2 T. An, Y. Wang, J. Tang, W. Wei, X. Cui, A. M. Alenizi, L. Zhang and G. Zheng, *J. Mater. Chem. A.*, 2016, **4**, 13439-13443.
3 Y. Li, T. Bo, S. Zuo, G. Zhang, X. Zhao, W. Zhou, X. Wu, G. Zhao, H. Huang, L. Zheng, J. Zhang, H. Zhang and J. Zhang, *Angew. Chem. Int. Ed*., 2023, **62**, e202309341.
4 X. Liu, J. Meng, K. Ni, R. Guo, F. Xia, J. Xie, X. Li, B. Wen, P. Wu, M. Li, J. Wu, X. Wu, L. Mai and D. Zhao, *Cell Reports Physical Science*, 2020, **1**, 100241.
5 Y. Cao, K. Geng, H. Geng, H. Ang, J. Pei, Y. Liu, X. Cao, J. Zheng, and H. Gu, *Nano-Micro Lett.*, 2019, **11**, 15.
6 T. Zhu, S. Liu, B. Huang, Q. Shao, M. Wang, F. Li, X. Tan, Y. Pi, S.-C. Weng, B. Huang, Z. Hu, J. Wu, Y. Qian, and X. Huang, *Energy Environ. Sci*., 2021, **14**, 3194-3202.
7 C. Wang, and L. Qi, *Angew. Chem. Int. Ed*., 2020, **59**, 17219-17224.
8 L. Huang, D. Chen, G. Luo, Y.R. Lu, C. Chen, Y. Zou, C.L. Dong, Y. Li, and S. Wang, *Adv. Mater*., 2019, **31**, 1901439.
9 G. Zhou, M. Li, Y. Li, H. Dong, D. Sun, X. Liu, L. Xu, Z. Tian, and Y. Tang, *Adv. Funct. Mater.*, 2020, **39**, 1905252.
10 T. Wu, E. Song, S. Zhang, M. Luo, C. Zhao, W. Zhao, J. Liu, and F. Huang, *Adv. Mater.*, 2022, **34**, 2108505.
11 L. Qi, Z. Zheng, C. Xing, Z. Wang, X. Luan, Y. Xue, F. He, and Y. Li, *Adv. Funct. Mater*., 2021, **32**, 2107179.
12 J. Gautam, Y. Liu, J. Gu, Z. Ma, J. Zha, B. Dahal, L.N. Zhang, A.N. Chishti, L. Ni, G. Diao, and Y. Wei, *Adv. Funct. Mater*., 2021, **31**, 2106147.
13 H. Yan, Y. Xie, A. Wu, Z. Cai, L. Wang, C. Tian, X. Zhang, and H. Fu, *Adv. Mater*., 2019, **31**, 1901174.
14 Y. Wu, X. Tao, Y. Qing, H. Xu, F. Yang, S. Luo, C. Tian, M. Liu, and X. Lu, *Adv. Mater*., 2019, **31**, 1900178.
15 L. Guo, Q. Liu, Y. Liu, Z. Chen, Y. Jiang, H. Jin, T. Zhou, J. Yang, and Y. Liu, *Nano Energy*, 2022, **92**, 106707.
16 X. Shan, J. Liu, H. Mu, Y. Xiao, B. Mei, W. Liu, G. Lin, Z. Jiang, L. Wen, and L. Jiang, *Angew. Chem. Int. Ed*., 2019, **59**, 1659-1665.
17 S. Hao, L. Chen, C. Yu, B. Yang, Z. Li, Y. Hou, L. Lei, and X. Zhang, *ACS Energy Lett.*, 2019, **4**, 952-959.
18 J. Wang, M. Zhang, G. Yang, W. Song, W. Zhong, X. Wang, M. Wang, T. Sun, and Y. Tang, *Adv. Funct. Mater*., 2021, **31**, 2101532.
19 W. Hao, R. Wu, H. Huang, X. Ou, L. Wang, D. Sun, X. Ma, and Y. Guo, *Energy Environ. Sci*., 2020, **13**, 102-110.
20 Z. Kang, H. Guo, J. Wu, X. Sun, Z. Zhang, Q. Liao, S. Zhang, H. Si, P. Wu, L. Wang, and Y. Zhang, *Adv. Funct. Mater*., 2019, **29**, 1807031.